

www.acsami.org Research Article

Achieving Independent Control over Surface and Bulk Fluid Flows in Microchambers

Benjamin M. Tansi,[§] Raj Kumar Manna,[§] Oleg E. Shklyaev, Matthew L. Peris, Anna C. Balazs,* and Ayusman Sen*



Cite This: ACS Appl. Mater. Interfaces 2021, 13, 6870-6878



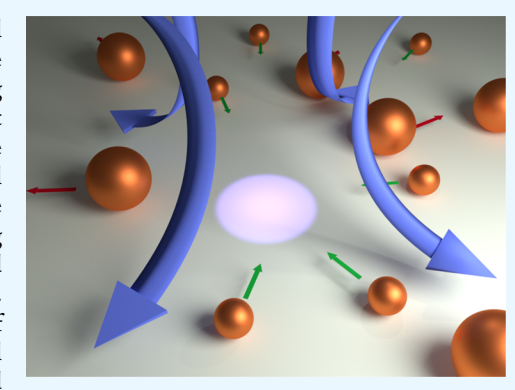
ACCESS

III Metrics & More



Supporting Information

ABSTRACT: To fully realize the potential of microfluidic platforms as useful diagnostic tools, the devices must be sufficiently portable that they function at the point-of-care, as well as remote and resource-poor locations. Using both modeling and experiments, here we develop a standalone fluidic device that is driven by light and operates without the need for external electrical or mechanical pumps. The light initiates a photochemical reaction in the solution; the release of chemical energy from the reaction is transduced into the spontaneous motion of the surrounding fluid. The generated flow is driven by two simultaneously occurring mechanisms: solutal buoyancy that controls the motion of the bulk fluid and diffusioosmosis that regulates motion near the bottom of the chamber. Consequently, the bulk and surface fluid flows can be directed independently of one another. We demonstrate that this exceptional degree of spatiotemporal control provides a new method for autonomously transporting different-sized particles in opposite directions within the chamber. Thus, one device can be used



to both separate the particles and drive them to different locations for further processing or analysis. This property is particularly useful for analyzing fluids that contain multiple contaminants or disease agents. Because this system relies on intrinsic hydrodynamic interactions initiated by a portable, small-scale source of light, the device provides the desired level of mobility vital for the next generation of functional fluidic platforms.

KEYWORDS: surface flows, bulk fluid flows, chemical pump, diffusioosmosis, flow reversal, particle sorting, microfluidics

1. INTRODUCTION

The advent of standalone and self-powered microfluidic platforms would permit assays for contaminants or disease agents to be performed in remote locations and resource-poor areas and thus enable realization of the full potential of these diagnostic tools. 1-8 To date, however, the majority of microfluidic devices require electrical input and mechanical pumps to drive the flow of fluids within the microchambers. Such attachments limit the use of these devices at the point-ofcare locations. One potential means of addressing the need for portability is to use light as the power source that drives the fluid flow. 10-12 The small-scale light source needed for these applications is easy to transport, adjust to a required intensity, and turn on and off to manipulate the fluid motion. 13 In recent studies, light was used primarily to generate heat by irradiating plasmonic nanoparticles or absorptive coatings within the microchambers and consequently prompt fluid flow through the mechanism of thermal buoyancy. 13,14 If, however, light could instigate additional mechanisms to drive flow, the flexibility and utility of the devices would be significantly enhanced.

Here, we use computational modeling and experimental studies to devise a light-activated approach that "pumps" fluid

flows without the need for external electrical or mechanical input. In particular, an external ultraviolet (UV) light source is used to illuminate a cylindrical region at the center of a reactant-filled chamber, as shown in Figure 1. The chemical reactions occur in the illuminated cylindrical region and generate fluid flow throughout the chamber. The light-driven pumping occurs *via* two different mechanisms: solutal buoyancy¹⁵ and diffusioosmosis. ^{16,17} Controlled by a single light source, the combination of these two mechanisms can generate two distinct streams of flowing fluid, which can flow in opposite directions within the chamber. Importantly, this behavior permits subtle manipulation of cargo submersed into the solution. Utilizing this approach, we create a system that enables particles of different sizes to move independently in different directions within the fluidic chambers. This size-dependent directionality can be particularly important for

Received: November 30, 2020 Accepted: January 22, 2021 Published: February 2, 2021





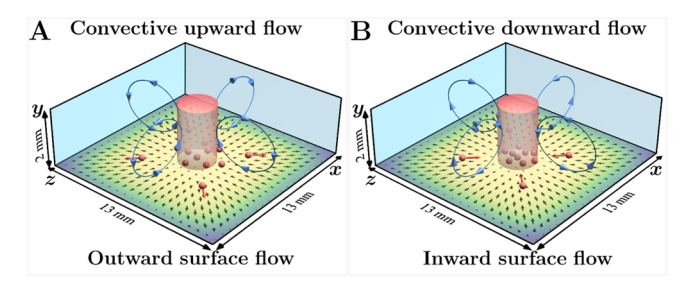


Figure 1. Schematic of convective fluid motion (marked by the blue arrows in the contour lines) driven by the photothermal and photochemical effects. These processes occur in the region exposed to the beam of the UV light (marked by the red cylindrical region). (A) Convective fluid motion is upward in the illuminated region (toward the center of the chamber at the bottom surface) and fluid flow directed by diffusioosmosis at the bottom surface (black arrows) drives the tracer particles (red spheres) in the direction opposite to the convective fluid flow (blue contour lines). (B) Convective fluid motion is downward in the illuminated region (away from the center at the bottom surface) and fluid flow directed by diffusioosmosis at the bottom surface drives the tracer particles toward the center of the illuminated region.

analyzing solutions that contain multiple impurities or infectious components. 18

The solutal buoyancy mechanism noted above dominates the behavior of the bulk fluid. 19,20 This mechanism is operative when the volume (and hence density) of the reactants is different from the volume of the products of a reaction. The expansion coefficient, β_i , quantifies the change in the local density of the fluid due to the presence of species i. This variation in the local density gives rise to a force that acts on the fluid and generates the spontaneous flow of the solution. When the density of the reactants is greater than the density of the products, the generated flow is referred to as "inward" flow or "upward pumping" (Figure 1A). In this case, the less dense, product-rich fluid rises to the top of the chamber; this behavior is analogous to the less dense fluid moving upward in the case of thermal buoyancy. The characteristic convective rolls culminate in "inward" flows that move toward the illuminated region along the bottom wall. On the other hand, when the reactants are less dense than the products, the product-rich fluid flows "outward", away from the center of the illuminated region (Figure 1B). Due to the continuity of the fluid, this flow eventually recirculates and moves downward from the top of the channel, as shown in Figure 1B, and hence is also referred to as "downward pumping".

For sufficiently slow fluid flows, the distribution of the chemicals across the domain, along with the fluid density, is determined not only by β_i but also by the relative diffusivities D_i of the chemicals. Moreover, for some combinations of β_i and D_i values, the fluid flow eventually changes direction. ^{12,20} As shown here, through the appropriate choice of chemical reactions, this switch in the directionality of the flow can be readily realized. These examples illustrate the level of spatiotemporal control that can be achieved over the flow in the bulk of the fluid.

Our system also relies on fluid flow directed by diffusioosmosis, which occurs along a surface in response to a gradient of chemical species (whether charged or uncharged). In essence, diffusioosmosis becomes evident near solid boundaries as the advective transport reduces to zero and diffusion begins to dominate.

In the studies described below, our system takes advantage of both the above mechanisms to create distinct flow streams that can change direction over time and eventually move in opposite directions within one chamber. To illustrate the governing principles in our approach, we focus on the sequential oxidation of alcohols in solution with hydrogen peroxide (H₂O₂) under UV irradiation. The light dependence of this process allows us to focus exclusively on the reactions occurring within the illuminating beam. Below, we first detail the kinetics of the chemical reactions considered here. We then present the results of the computational studies and the complementary experimental findings, which helped inform choices made in the computational modeling and confirmed the results from the simulations.

2. REACTION KINETICS

We specifically focus on the chemical reactions in an aqueous mixture containing 0.217 M ethanol (C_2H_5OH) and 0.49 M hydrogen peroxide (H_2O_2) in the presence of UV light that lead to the production of acetic acid²¹ (CH_3COOH). For numerical simplicity, we neglect fast intermediate reaction steps and explicitly model the production of acetaldehyde (C_4GH_3CHO), paraldehyde ($C_6H_{12}O_3$), and acetic acid (CH_3COOH), which occur by the following steps.

$$C_2H_5OH + H_2O_2 \xrightarrow{k_1} CH_3CHO + 2H_2O$$
 (1a)

$$3CH_3CHO \underset{k_3}{\overset{k_2}{\rightleftharpoons}} C_6H_{12}O_3 \tag{1b}$$

$$CH_3CHO + H_2O_2 \xrightarrow{k_4} CH_3COOH + H_2O$$
 (1c)

In the first equation (eq 1a), k_1 is the rate constant that accounts for transformations of ethanol and hydrogen peroxide into acetaldehyde. We assume that this constant already includes the effect of the UV light, which enables the photolysis of hydrogen peroxide (H₂O₂) into two hydroxyl radicals (OH) and the subsequent reaction with ethanol (C₂H₅OH).²² The nuclear magnetic resonance (NMR) spectra obtained in the experiments indicate the presence of paraldehyde, a denser cyclic trimer of acetaldehyde (see Section 4 and Supporting Information Table S1), which plays the main role in developing the directionality of the buoyancydriven flows. Therefore, we explicitly model the chemical equilibrium (eq 1b) controlled by the rate constants k_2 and k_3 that account for the oligomerization of acetaldehyde to paraldehyde and reverse deoligomerization of paraldehyde to acetaldehyde. In the final step (eq 1c), the rate constant k_4 accounts for the formation of acetic acid from the reaction between acetaldehyde and hydrogen peroxide.

To describe the transformations of the chemicals that participate in eqs 1a, 1b, and 1c, we use the following kinetic equations

$$\frac{d[C_2H_5OH]}{dt} = -k_1[C_2H_5OH][H_2O_2]$$
 (2a)

$$\frac{\frac{d[H_2O_2]}{dt}}{dt} = -k_1[C_2H_5OH][H_2O_2] - k_4[CH_3CHO][H_2O_2]$$
(2b)

$$\begin{split} \frac{\frac{\text{d[CH}_3\text{CHO]}}{\text{d}t} &= k_1 [\text{C}_2\text{H}_5\text{OH}][\text{H}_2\text{O}_2] - k_4 [\text{CH}_3\text{CHO}][\text{H}_2\text{O}_2] \\ &- k_2 [\text{CH}_3\text{CHO}] + k_3 [\text{C}_6\text{H}_{12}\text{O}_3] \end{split}$$

(2c)

$$\frac{d[C_6H_{12}O_3]}{dt} = k_2[CH_3CHO] - k_3[C_6H_{12}O_3]$$
 (2d)

$$\frac{\mathrm{d}[\mathrm{CH_3COOH}]}{\mathrm{d}t} = k_4[\mathrm{CH_3CHO}][\mathrm{H_2O_2}] \tag{2e}$$

The chemical species consumed and produced during the reactions in eqs 1a, 1b, and 1c yield different solutal volumes and, therefore, alter the local density of fluid. Below, we describe our model for the resultant solutal buoyancy effects.

3. COMPUTATIONAL MODEL

3.1. Solutal Buoyancy. The local density changes in the fluid due to the presence of paraldehyde, acetaldehyde, and acetic acid give rise to the solutal buoyancy mechanism, which is important for pumping the fluid within the column of light. We begin by considering the fluid pumping of the bulk solution. For compactness, we denote the reactants C₂H₅OH, H_2O_2 , CH_3CHO , $C_6H_{12}O_3$, and CH_3COOH by the indexes i =1, ..., $N_{\rm C}$, with $N_{\rm C}$ = 5. The local variations in the density $\rho({\bf r},t)$ of the aqueous solution that occur at the coordinate $\mathbf{r} = (x,y,z)$ and time t in response to changes in the concentrations $C_i(\mathbf{r},t)$ of $N_{\rm C}$ reactants can be approximated as $\Delta \rho({\bf r},\,t)=\rho_0 \sum_i^{N_{\rm C}} \beta_i C_i$ where ρ_0 is the solvent density, and $\beta_i = \frac{1}{\rho_0} \frac{\partial \rho}{\partial C_i}$ are the corresponding solutal expansion coefficients. Since the temperature changes due to the chemical reactions considered here are small and the thermal expansion coefficients are significantly smaller than the solutal expansion coefficients, we ignored the effect of the thermal buoyancy.

The density variations in the solution give rise to a buoyancy force per unit volume $\mathbf{F}_b = \mathbf{g} \rho_0 \sum \tilde{\beta_i} C_i$, where \mathbf{g} is the gravitational acceleration. This buoyancy force generates the fluid motion characterized by the velocity $\mathbf{u}(u_{xy}u_{yy}u_{z})$.

To simulate the chemical transformations (eqs 2a, 2b, 2c, 2d, and 2e), their transport, and the resulting fluid motion, we use a rectangular domain of dimensions $\Omega = \{(x,y,z):-L/2 \le$ $x,z \le L/2$, $0 \le y \le H$ }. The domain is illuminated from below by the UV light with a beam of the radius R focused at the center of the domain (Figure 1). Following the experimental geometry, we choose a fluidic domain of size $L \times \tilde{H} \times L$ with horizontal dimension L = 13 mm, height H = 2 mm, and radius of the UV light beam R = 2 mm. We assume that the intensity of the light is uniform over the cross section of the beam, which promotes the chemical reactions given in eqs 1a, 1b, and 1c. The fluid motion and the dynamics of the dissolved chemicals C, are described by the continuity, Navier-Stokes (in the Boussinesq approximation²³), and reaction-diffusion equations

$$\nabla \cdot \mathbf{u} = 0 \tag{3}$$

$$\frac{\partial \mathbf{u}}{\partial t} + (\mathbf{u} \cdot \nabla)\mathbf{u} = -\frac{1}{\rho_0} \nabla p + \nu \nabla^2 \mathbf{u} + \mathbf{g} \sum_i \beta_i C_i$$
(4)

$$\frac{\partial C_i}{\partial t} + (\mathbf{u} \cdot \nabla)C_i = D_i \nabla^2 C_i \pm Q_i f(r)$$
(5)

Here, ν is the kinematic viscosity of the fluid, ∇ is the spatial gradient operator, D_i are the diffusivities of the reactants i = 1,

..., N_C , and Q_i are the reaction rate terms given by the righthand sides of eqs 2a, 2b, 2c, 2d, and 2e. We assume that the chemical reactions occur in the region of the domain exposed to the beam of the UV light with the radius R and described by the function

$$f(x, y, z) = \begin{cases} 1, & \text{if } (x^2 + z^2) \le R^2; \ 0 < y < H \\ 0, & \text{otherwise} \end{cases}$$
 (6)

We use no-slip boundary conditions for fluid velocities and impose no chemical flux across the walls of the domain

$$\{x, z\} = -L/2, L/2:$$
 $\mathbf{u} = 0, \frac{\partial C_i}{\partial n} = 0$ $y = 0, H:$ $\mathbf{u} = 0, \frac{\partial C_i}{\partial n} = 0$

Here, $\hat{\mathbf{n}}$ is the unit normal vector at walls pointing into the fluid domain.

We numerically solve eqs 3 and 4 using the lattice Boltzmann method for fluid dynamics. The reaction-diffusion equation (eq 5) is solved using a finite-difference method. Here, considering the symmetry of the problem, we choose a computational domain of size $53\Delta x \times 53\Delta x \times 9\Delta x$, where Δx is taken to be 250 μ m.

The diffusivities D_i and expansion coefficients β_i for the reactants $i = 1, ..., N_C$ (C₂H₅OH, H₂O₂, CH₃CHO, C₆H₁₂O₃, and CH₃COOH) participating in the reactions in eqs 1a, 1b, and 1c, are provided in the Supporting Information Table S1. The reaction rate constants used in the simulations were calibrated to reproduce the experimental observations and thus were set to $k_1 = 2.5 \times 10^{-5} \text{ s}^{-1} \text{ M}^{-1}$, $k_2 = 5.2 \times 10^{-4} \text{ s}^{-1}$, $k_3 = k_2/15$, and $k_4 = 6.25 \times 10^{-4} \text{ s}^{-1} \text{ M}^{-1}$. (Note that our rate constants k_i implicitly include the fact that the reactions occur only in the central region described by the function $f(\mathbf{r})$ in eq

As indicated further below, the above rate constants allowed us to reproduce the experimentally observed values of the chemical concentrations $\langle C_i \rangle = \frac{1}{L^2 H} \int C_i(\mathbf{r}, t) d\mathbf{r}$, averaged over the hybridization chamber, and fluid velocity $\mathbf{u}(x,y,z,t)$, measured at the position x = 0.75 mm, y = 0.5 mm, and z =0 mm.

3.2. Diffusioosmosis. While the bulk solution is driven by solutal buoyancy effects, fluid near the surface is directed by diffusioosmosis. In this case, the relevant species are the dissociation products of acetic acid (acetate and hydrogen ions). For solutions of symmetrically charged binary electrolytes, the fluid velocity generated along the wall by diffusioosmosis can be presented as 24,25

$$\mathbf{u}^{S} = \gamma \left(\frac{\nabla_{\parallel} C}{C}\right),$$

$$\gamma = \frac{\varepsilon}{4\pi\eta} \left(\beta_{O} \zeta^{\frac{k_{B}T}{Ze}} + \frac{1}{8} \zeta^{2} [1 - 2(1 - \beta_{O}^{2})]\right)$$
(7)

Here, $\nabla_{\parallel}C$ denotes the concentration gradient parallel to the wall; $\varepsilon = 4\pi\varepsilon_0\varepsilon_r$, where $\varepsilon_0 = 8.85 \times 10^{-12} \text{ C V}^{-1} \text{ m}^{-1}$ is the vacuum permittivity and $\varepsilon_{\rm r}=80$ is the relative permittivity of water. $\eta=8.94\times 10^{-4}~{\rm kg~m^{-1}~s^{-1}}$ is the dynamic viscosity of water. $\zeta = -43$ mV is the zeta potential of the surface. $e = 1.6 \times 10^{-2}$ 10^{-19} C is the elementary charge and Z = 1 is the electrolyte valence. $k_{\rm B} = 1.38 \times 10^{-23}$ J K⁻¹ is the Boltzmann constant and T = 293 K is the absolute temperature. $\beta_{\rm O} = (D^+ - D^-)/(D^+ +$ D^{-}), where D^{+} and D^{-} are the diffusivities of the positive and

negative ions, respectively. Assuming that acetic acid dissociates into the acetate and a hydrogen ion CH₃COOH \rightleftharpoons CH₃CO₂ $^-$ + H⁺, we calculate $\beta_{\rm O}=0.795$, where the diffusivities of positive and negative ions are set to $D^+=D_{\rm H^+}=8.66\times 10^{-9}~\rm m^2/s$ and $D^-=D_{\rm CH_3CO_2}^-\approx D_{\rm CH_3COOH}=0.989\times 10^{-9}~\rm m^2/s$, respectively. Given the higher diffusivity of the hydrogen ion, the electric field points inward. Provided a negatively charged surface, the near-surface flow should also be directed inward, opposite to the direction of bulk flow. (In the case of a positively charged surface, the near-surface flow would shift to outward.)

To analyze the details of the fluid flows and particle dynamics near the bottom wall, we develop a two-dimensional (2D) lubrication model, $^{26-28}$ which is detailed within the Supporting Information. In particular, we use the fact that the fluid velocities were experimentally observed to be slow, that is, $u\sim 10^{-6}$ m/s, and treat the problem in the limit of a small Reynolds number (Re = $\frac{Lu}{\nu}\sim 10^{-3}$ for $L\sim 10^{-3}$ m, $\nu\sim 10^{-6}$ m²/s). In this model, we use the diffusive time scale $\tau=H^2/D_2$; the expansion coefficients and reagent diffusivities are taken from Table S1. The reaction rate constants in the 2D simulations are set to $k_1=2.5\times 10^{-5}$ s $^{-1}$ M $^{-1}$, $k_2=5.2\times 10^{-4}$ s $^{-1}$ m $^{-1}$ and are different from the values used for 3D simulations above due to changes in the geometry of the illuminated region, which in the case of 2D system is infinitely extended along the z-direction.

4. EXPERIMENTAL APPROACH

The experimental setup was designed to match the system described above, with the exception that the domain was circular (height = 2 mm, diameter = 13 mm) rather than square. An aqueous solution of $C_2H_5OH~(0.217~M)$ and $H_2O_2~(0.49~M)$ was added to the chamber and irradiated with a beam of UV light having a diameter of 2 mm and an intensity of 780 mW/cm². In a typical experiment, the motion of suspended tracer particles (3 μm carboxylate-functionalized polystyrene) was observed at one-quarter of the chamber height (500 μm) and seen to briefly move toward the illuminated center before changing direction after approximately 90 s (Supporting Information Video 1). The in-plane velocities over time are denoted by the markers in Figure 2B and are seen to match closely with the computational values.

The reaction products were characterized and monitored by a combination of ¹H and ¹³C NMR spectroscopy. From these spectra, it was evident that acetaldehyde, paraldehyde, and acetic acid were being produced (Figures S1–S3). The exact concentration of these species could be determined by adding sodium trimethylsilylpropanesulfonate (DSS) as a reference standard (Figure 2A). Importantly, no reaction was observed without UV light or without hydrogen peroxide.

The production of acetic acid was further confirmed by a sharp decrease in pH over time (Figure S4). A commensurate decrease also occurred when acetaldehyde was used as the starting material in place of ethanol. For comparison, isopropyl alcohol was tested under these same conditions and the pH did not vary from its initial value. It also did not promote downward pumping, and instead, the solution moved upward. This result speaks to the need for primary alcohols to drive downward pumping in the manner described. Secondary alcohols react to yield ketones; unlike aldehydes, ketones are resistant to further oxidation. A suite of other analytes was tested to support this assertion; the results of these tests are given in Table 1. To confirm that the reversal was due to density, another experiment was performed with 150 mM sodium sulfate in order to quench any electrokinetic effects (Figure S5). Glycerol was used for this experiment since it demonstrated the highest downward pumping rate. The flow reversal occurred despite the addition of salt. Note that

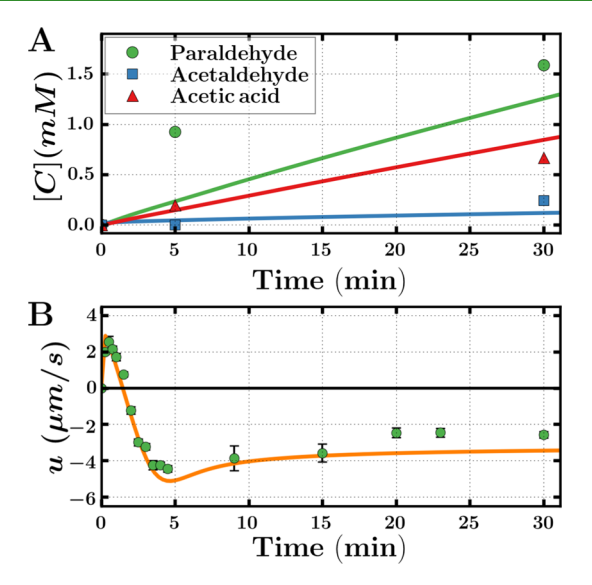


Figure 2. Experimental (markers) and simulation (lines) results for the system of ethanol (0.217 M) and hydrogen peroxide (0.49 M) under irradiation by UV light. (A) Concentration of reaction products over time as determined by NMR. (B) The velocity of 3 μ m polystyrene tracer particles was measured at one-quarter of the cell height and 700 μ m from the flow center. Negative values denote outward motion resulting from the observed downward convection.

Table 1. Observed Pumping Rates of a Suite of Tested Compounds a

compound	rate $(\mu m/s)$
glycerol	-6.4 ± 0.6
methanol	-4.5 ± 0.3
formaldehyde	7.0 ± 0.6
formic acid (pH 2)	5.4 ± 0.4
ethanol	-4.3 ± 0.3
acetaldehyde	5.7 ± 0.4
acetic acid	4.6 ± 0.5
isopropanol	4.9 ± 0.4
H_2O_2	7.2 ± 0.6

"Downward pumping is denoted by negative values. The concentration of each compound was 0.217 M and hydrogen peroxide was kept at 0.49 M for each. The $\rm H_2O_2$ only trial had a concentration 0.49 M. The rates were monitored at 500 μm above the surface by observing 3 μm polystyrene-carboxylate tracer particles.

the oxidation reactions are exothermic, thereby ruling out cooling as the source of downward pumping. More detailed experimental details are provided in the Supporting Information.

We used the above computational and experimental approaches to generate Figure 2, which provides a comparison of the results from the simulations and the experiments. The experimental data is indicated by the symbols in Figure 2A,B, while the simulation data for the corresponding values of the chemical concentrations, $\langle C_i(\mathbf{r},t)\rangle$, and flow velocities, $\mathbf{u}(\mathbf{r},t)$, are indicated by the solid lines. Notably, the computational values match closely with the experimental values. Moreover, both the computational and experimental data reveal a change in the sign of the velocity (Figure 2B), indicating that the fluid flow changes direction with time. In particular, the plots indicate that the movement of the fluid eventually changes from inward (positive \mathbf{u}) to outward (negative \mathbf{u}) flow. Using this experimentally validated model, we obtained the results described in the following section.

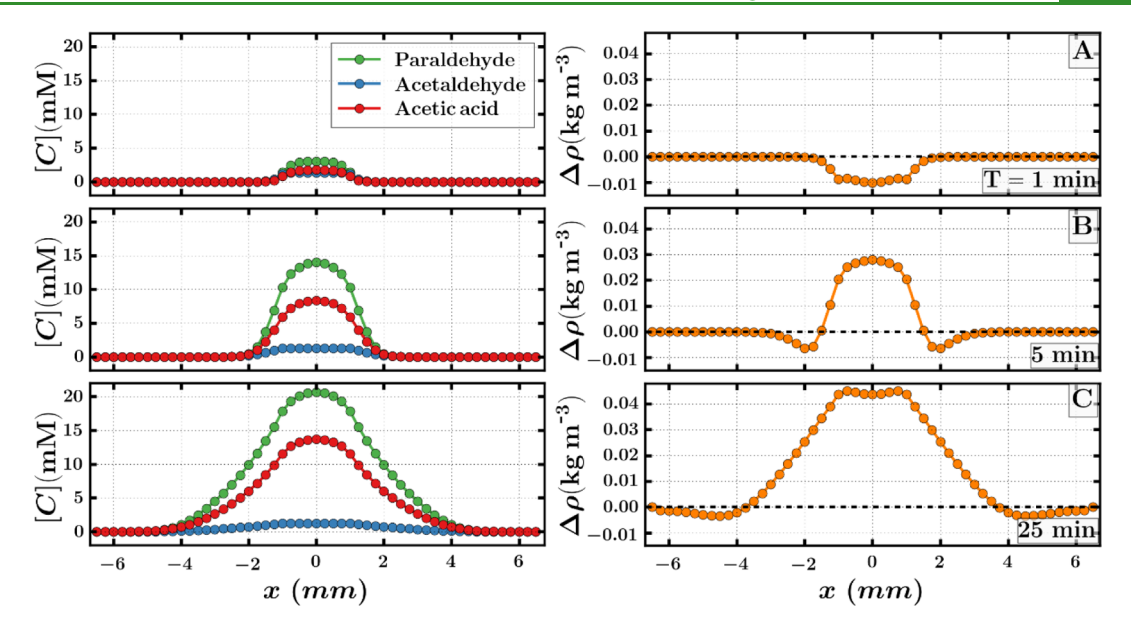


Figure 3. Changes in the chemical compositions and density of the solution with time. Left panels show the chemical concentrations along the section y = 0.5 mm and z = 0 for three different instances of time. Right panels show the corresponding variations in the density of the solution $\Delta \rho(\mathbf{r}, t) = \rho_0 \sum_{i=0}^{N_C} \beta_i C_i$ along the same section.

5. RESULTS AND DISCUSSION

5.1. Evolution of Buoyancy-Driven Flow. The light-activated chemical reactions in the center of the domain (eqs 1a, 1b, and 1c) enable the chemomechanical transduction that ultimately leads to the fluid motion. In particular, the heterogeneous chemical composition of the solution generated by the reactions gives rise to the transport of the reactants in the radial direction. Importantly, both the computational and experimental data indicate that the fluid flow changes direction with time (Figure 2B), moving from an initially inward flow to an eventually outward flow.

The chemical fluxes $J_i = D_i \nabla C_i + \mathbf{u} C_i$ that enable the transport include the respective diffusive and advective contributions. For sufficiently slow fluid flows, the advection can be neglected and the distribution of the chemicals across the domain, along with the fluid density, is determined by the relative diffusivities D_i of the chemicals. In this case, the direction of the fluid flow is determined²⁰ by specific combinations of the diffusivities D, and expansion coefficients β_i of the participating reactants i. The underlying mechanism of the flow reversal is the change in the sign of density variation $\Delta \rho(\mathbf{r}, t) = \rho_0 \sum_{i}^{N_{\rm C}} \beta_i C_i$ over time. During the chemical reactions, if the sign of the density variation, $\Delta \rho({\bf r},t)$, at the center of domain changes from positive (denser fluid) to negative (lighter fluid), then the direction of the fluid flow changes direction from outward to inward flow. Prior studies²⁰ revealed that depending on the relative diffusivity $\delta = D_p/D_R$ and expansion coefficient $\beta = \beta_P/\beta_R$ of the products and reactants in the solution, the fluid flow can change direction over time. Here, $D_{\rm p}$ and $D_{\rm R}$ are the average diffusivities and $\beta_{\rm p}$ and β_R are the average expansion coefficients of products and reactants, respectively (see Table S2). In particular, 20 the inward fluid motion at early times turns to outward motion at later times when δ < 1 and δ < β . Similarly, when δ > 1 and δ > β , the flow reversal occurs from the outward flow at early times to inward motion at later time moments.

We use parameters from Table S2 to calculate average diffusivities and expansion coefficients for the chemical

solution before and after the chemical reactions listed in eqs 1a, 1b, and 1c. Therefore, for the corresponding relative diffusivity and the expansion coefficient (δ = 0.75 and β = 3.8), we anticipate that the flow reverses from the inward to outward direction. This behavior is indeed seen in Figure 2B.

Numerical solution of eqs 3–5 yields the evolution of the chemical products generated through reactions in eqs 1a, 1b, and 1c. The left panels in Figure 3 show the concentrations for paraldehyde, acetaldehyde, and acetic acid (in green, blue, and red, respectively) calculated along the section y = 0.5 mm and z = 0 for three different times. The corresponding densities of the chemical solution for the same times are shown on the right panels in Figure 3. Figure 4 displays details of the fluid flow generated by the density distributions presented in the right panel in Figure 3.

At early times (1 min after the start of the reaction), the chemical solution has a lower density in the central region, as shown on the right panel in Figure 3A. The resulting buoyancy force drives the fluid upward in the central region and toward the center along the bottom wall, as shown in Figure 4. At late times (>2.5 min), the distribution of the chemicals along the chamber changes (left panel in Figure 3) and the solution becomes denser in the center of the domain (corresponding right panels in Figure 3B,C). As a result, the fluid flow changes direction and shows outward motion away from the irradiated central region (Figure 4B,C). In both experiment and simulations, the flow reversal from inward to outward motion occurred around 2 min after the start of the reaction. The dynamics of the reagent concentrations $c_i(t,x)$ (not shown) and related fluid density are qualitatively similar to those presented in Figure 3.

5.2. Contributions from Different Mechanisms of Induced Flow. Our 2D lubrication model^{26–28} (detailed in the Supporting Information) allows us to further validate the above predictions from the 3D computer simulations and gain additional insights into the fluid dynamics near the bottom wall. While this lubrication model is a more coarse-grained approach (see Section 3.2) than our computational method

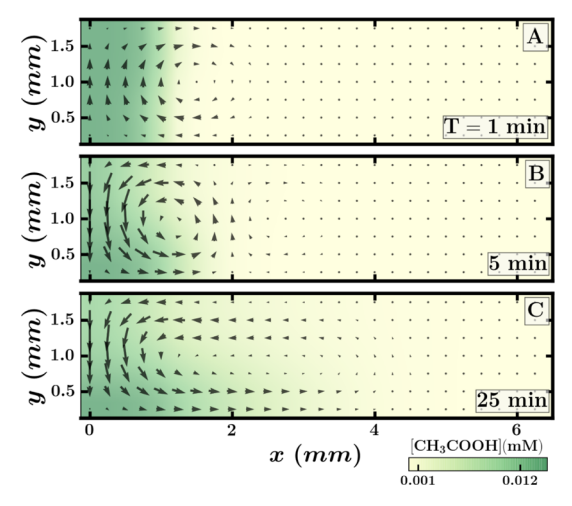


Figure 4. Fluid flow reversal resulting from the chemical reaction of ethanol and hydrogen peroxide promoted by the UV light. (A) At early time, 1 min, the fluid flows upward in the center of the irradiated region $(-1 \text{ mm} \le x \le 1 \text{ mm})$. (B,C) The fluid flows downward at 5 (B) and 25 min (C). Black arrows indicate the direction and magnitude of the fluid flow, and the color bar indicates the concentration of acetic acid (CH₃COOH) in the solution. The flow structure is shown in the right half $(x \ge 0)$ of the domain for the cross section at z = 0.

described in Section 3.1, it explicitly includes the effect of diffusioosmotic flow through the slip boundary conditions at the bottom wall. Hence, this lubrication model explicitly takes into account the net effects of both solutal buoyancy and diffusioosmosis. Using this model, we calculated the net flow velocities near the bottom wall (see the Supporting Information). These results (Figure 5) also indicate the reversal of the fluid flow due to the chemical reactions promoted by the UV light in the central region of the chamber and thus confirm the predictions from the simulations

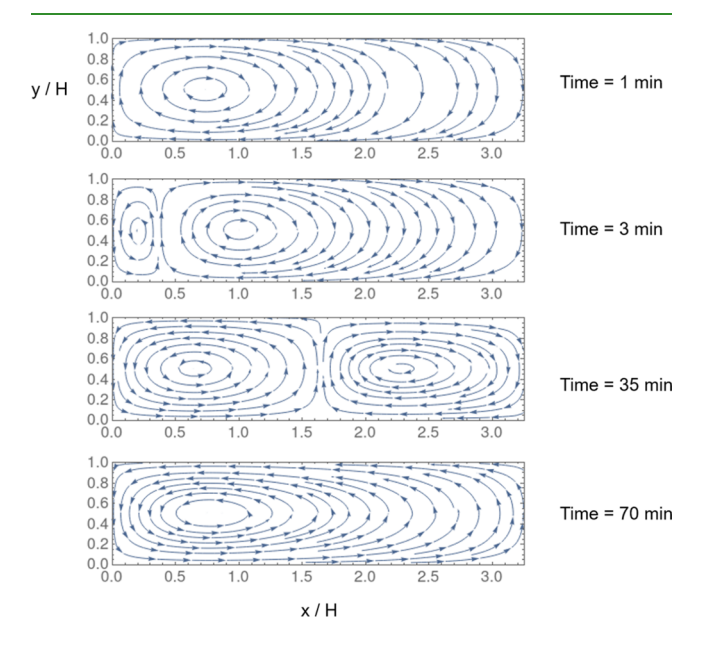


Figure 5. Fluid flow reversal in 2D lubrication approximation. The inward flow in the central region at early times turns into the outward flow at later times. Panels from top to bottom show a sequence of flow structures as time increases. Arrows indicate local flow directions. The scale $H=2\,\mathrm{mm}$.

described above. In particular, the plots show that at early times, the flow in the central region ($x \approx 0$) is inward, while at later times, the flow is outward.

Through the lubrication model, we can calculate the relative contributions from the buoyancy-driven flow (green lines) and diffusioosmotic flow (red line) to the generated fluid flow (blue lines). Figure 6A-C shows that while buoyancy-driven flow changes direction with time, the flow due to diffusioosmotic remains directed toward the center near the bottom wall. The net horizontal flow, u, given by eq S6 is plotted in Figure 6C. The details of the flow close to the bottom wall are shown in Figure 6D. Near the wall, the flow is dominated by the diffusioosmosis and directed toward the illuminated center, while further from the wall, the flow is dominated by the solutal buoyancy, and the flow points away from the illuminated center at late times, as predicted by the ratios of the diffusivities and expansion coefficients (i.e., δ = 0.75 and β = 3.8). As discussed below, these findings are corroborated through the experimental studies and yield a novel mechanism for controlling the trafficking of differentsized particles in the chamber.

5.3. Experiments to Probe Behavior Near the Surface. To complement and validate our modeling studies, we performed the following experiments to test the near-surface effects. We used a solution containing glycerol since this system demonstrated the strongest downward pumping (Table 1) and, like ethanol, produced acid products (pH 7.4 \pm 0.03 to 3.87 ± 0.07 after 1 h). In agreement with theoretical predictions, tracer particles along the surface migrated inward, opposite to the direction of the bulk flow (Supporting Information Video 2). To confirm that this motion was derived from diffusioosmosis, a cationic surfactant (0.1 mM cetyltrimethylammonium bromide, CTAB) was added to the solution to change the sign of the surface charge. In particular, with the addition of CTAB, the zeta potential changed from -35 ± 4 to $+43 \pm 5$ mV. The direction of particle motion along the surface switched from inward to outward, reflecting the change in near-surface fluid transport, as anticipated from the model. We note that the related phenomenon, diffusiophoresis, would cause the tracer particles to exhibit the opposite behavior to that observed. The polystyrene carboxylate particles used in these experiments have a negative surface charge and would therefore move outward if this were the dominant effect. This is true as long as the cationic product has a higher diffusivity than its counterion.

In a similar manner, fluid pumping could be directed upward, while near-surface flows moved outward. This was accomplished by performing the experiment with acetaldehyde, H₂O₂, and CTAB. Under UV irradiation, a solution of acetaldehyde and H₂O₂ will pump upward (Table 1) while still yielding acetic acid (Figure S4). Diffusioosmosis will occur due to the acid product, and given the addition of CTAB, this flow will be directed outward against the pumping direction of the bulk. This is demonstrated by the smaller particles (10 μ m polystyrene-carboxylate) in Supporting Information Video 3. In contrast to the ethanol system, the bulk pumping direction, in this case, is upward. This is mainly due to the difference in the local production of paraldehyde in these two systems. The local production of paraldehyde in the ethanol system is a key factor for the increase of the local density that drives the downward pumping of the fluid. In the acetaldehyde system, however, paraldehyde is already present in equilibrium with

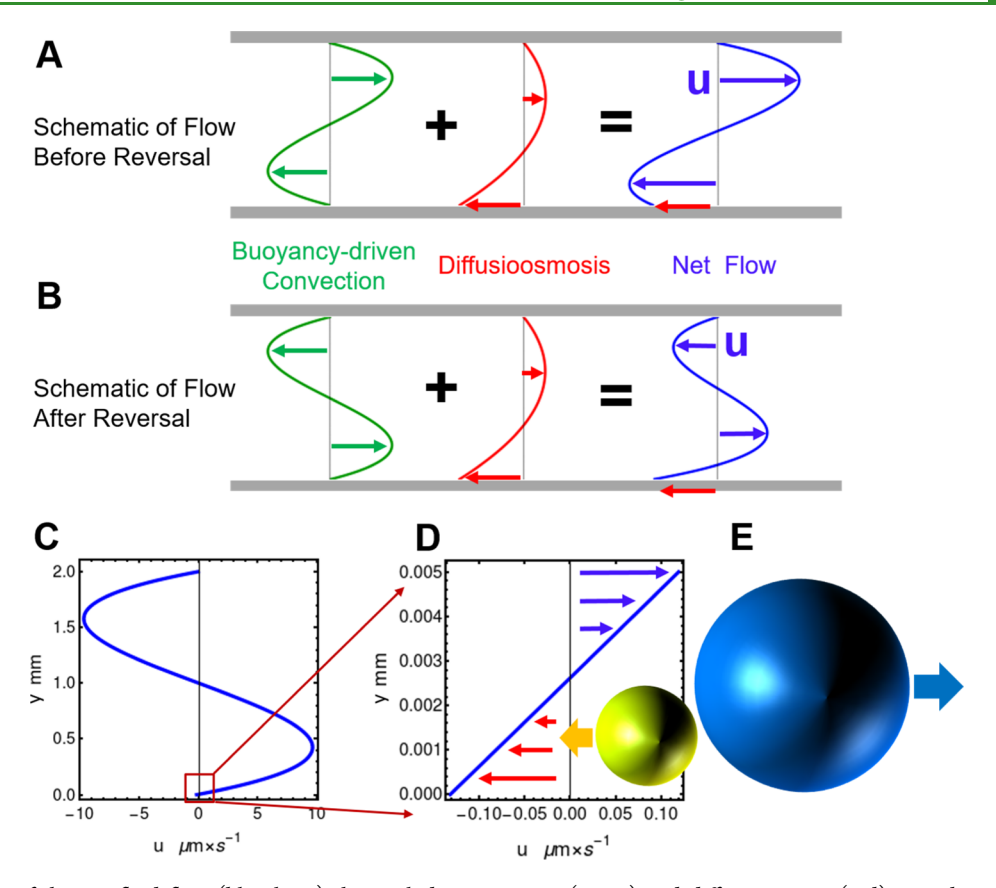


Figure 6. Structure of the net fluid flow (blue lines) that includes convective (green) and diffusioosmotic (red) contributions. (A) Schematic composition of the net flow (blue) at an early time before the flow reversal. (B) Schematic composition of the net flow (blue) at a later time after the reversal. (C) Flow profile u(x,y,t) given by eq S15 for x = 0.75 mm and t = 15 min. (D) Details of the fluid flow near the bottom wall. The flow is dominated by the diffusioosmotic contribution (red arrows for y < 0.0025 mm) next to the wall. Further from the wall, the flow is dominated by the solutal buoyancy convection (blue arrows for y > 0.0025 mm). (E) Sufficiently small particles (yellow) are dragged by the diffusioosmotic flow to the left, while large particles (blue) are controlled by the fluid drag imposed by the buoyancy-driven flow.

acetaldehyde and does not contribute to the local density change.

These experiments yield two important findings. First, they demonstrate a method to promote directed pumping, and second, they establish a means to affect the direction of multiple flow regimes independently of one another. Both these properties enable the application described below.

Due to the narrow region over which diffusioosmosis dominates, the direction of settled tracer particles exhibit sizedependent behavior. The image in Figure 6E reveals how the above behavior can be used to regulate size-dependent motion of particles immersed in the solution. Namely, the calculations predict that the dynamics of sufficiently small particles (yellow in Figure 6E) is dominated by diffusioosmosis, while larger particles (blue in Figure 6E) are dragged by buoyancy-driven convection. When the bulk solution and near-surface flows are opposite of one another, the direction of particle migration relies on the relative contribution of the two flows to the particle drag. In the system with acetaldehyde, H₂O₂, and CTAB, large particles effectively feel the bulk flows to a greater extent and hence move inward, in accordance with the bulk fluid pumping. Smaller particles are instead subject to nearsurface flows and continue to move outward against the direction of bulk pumping (Supporting Information Video 3), as shown in Figure 7. In this example, 10 and 20 μ m carboxylate-functionalized polystyrene particles were observed

to migrate in opposite directions on the bottom surface of the chamber.

It is important to acknowledge the particle size and charge dependence in diffusiophoresis. It has been shown that size will

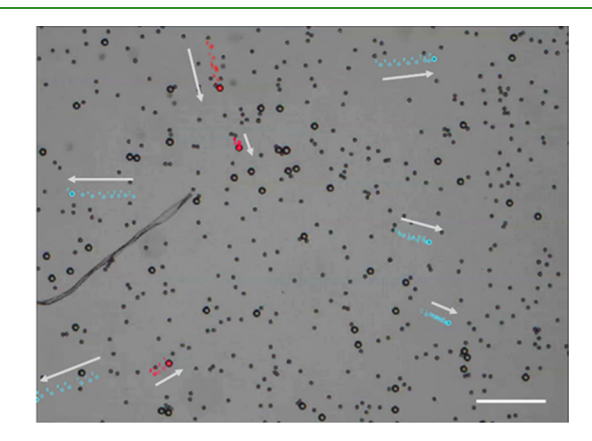


Figure 7. Surface migration of 10 and 20 μ m tracer particles during the upward pumping of acetaldehyde/ H_2O_2 solution with added CTAB under irradiation. The red tails represent the motion of 20 μ m particles as they move inward toward the irradiation center. Blue tails are of the 10 μ m tracer particles moving outward, responding to near surface gradients (see Video S3). Due to the high concentration of CTAB, there is significant sticking at a short time scale near the surface. Scale bar = 200 μ m.

affect diffusiophoretic mobility but only if the Debye layer is comparable to the size of the particle, $^{29-31}$ which is unlikely for $10-20~\mu m$ particles. Diffusiophoresis also depends on surface charge. The addition of CTAB changes the sign of the zeta potential for the particles (from -32 ± 1 to $+38.8\pm0.4$ mV). Thus, if diffusiophoresis dominated over diffusioosmosis, we would expect the $10~\mu m$ particles to migrate inward rather than outward.

6. CONCLUSIONS

Combining modeling and experiments, we developed a microfluidic platform that spontaneously generates self-sustained fluid flow and simultaneously exhibits autonomous control over the directionality of the generated flow. A light source is used to initiate photochemical reactions in the chamber; the release of chemical energy from the reactions is transduced into the motion of the surrounding fluid. Hence, the device exhibits a form of photochemo-mechanical transduction that enables it to operate in a standalone fashion, without the need for external electrical or mechanical pumps.

The directionality of the flows is controlled by two inherent hydrodynamic mechanisms, which are operative in different portions of the chamber. The flow in the bulk of the fluid is driven by solutal buoyancy; the directionality of the bulk flow depends on the relative diffusivity $\delta = D_{\rm p}/D_{\rm R}$ and expansion coefficient $\beta = \beta_{\rm p}/\beta_{\rm R}$ of the products and reactants in the solution. With the appropriate choice of reactants, the flow changes direction with time, and this behavior is robust for a wide number of systems. The magnitude of the bulk fluid flow driven by solutal buoyancy is controlled by the dimensionless

Grashof number, $Gr = \frac{g \sum_i \beta_i C_i H^3}{\nu^2}$, and Rayleigh number,

$$Ra = \frac{g \sum_{i} \beta_{i} C_{i} H^{3}}{\nu D_{1}}$$
, where D_{1} is the diffusivity of the reactant 1.

The typical Grashof and Rayleigh numbers corresponding to the maximal fluid velocity (Figure 4C) are 3.5 and 2470, respectively. The flow velocities can be increased by either using chemicals with higher expansion coefficients, increasing the height of the chamber or increasing the initial concentration of chemicals.

The flow at the surface is driven by diffusioosmosis, which occurs along a charged surface as a result of unequal diffusivities within a gradient of ionic species. The directionality of this flow can be changed dynamically through the addition of reagents that modify the surface charge. We note that the contribution of the diffusioosmosis to the net flow is 1 order of magnitude (0.1 μ m/s) smaller than the bulk fluid flow $(4 \, \mu \text{m/s})$, as determined both numerically and experimentally. The flow velocities due to diffusioosmosis can be increased by increasing the zeta potential of the bottom surface or increasing the concentration gradients of the ions. Hence, by harnessing both solutal buoyancy and diffusioosmosis, we can direct the bulk and surface fluid flows independently of one another. We demonstrated that this novel interfacial behavior provides a new mechanism for directing the transport of different-sized particles along opposite directions. Thus, one device can be used to both separate the particles and drive them to different locations for further processing or analysis. This property is particularly useful for analyzing fluids that contain multiple particulate types or pathogens. Because this fluidic platform relies on intrinsic hydrodynamic interactions that are initiated by a portable, small-scale source of light, the

device is highly mobile. Consequently, it can be used at the point-of-care as well as in resource-poor or remote locations.

ASSOCIATED CONTENT

Solution Supporting Information

The Supporting Information is available free of charge at https://pubs.acs.org/doi/10.1021/acsami.0c21291.

Spontaneous pumping reversal in the system with 0.217 M ethanol and 0.49 M hydrogen peroxide under UV irradiation (MP4)

Inward migration with 0.217 M glycerol and 0.49 M hydrogen peroxide along the bottom surface under UV irradiation (MP4)

Opposite migration directions of settled particles based on size (MP4)

Simulation of pumping reversal in the system with 0.217 M ethanol and 0.49 M hydrogen peroxide under UV irradiation (MP4)

Methods; product determination by NMR, results of pH trial, and velocity measurements for salt controls; diffusioosmosis in the 2D model; physical properties of chemicals; and average diffusivities and expansion coefficients of reactants and products (PDF)

AUTHOR INFORMATION

Corresponding Authors

Anna C. Balazs — Department of Chemical Engineering, University of Pittsburgh, Pittsburgh, Pennsylvania 15213, United States; orcid.org/0000-0002-5555-2692; Email: balazs@pitt.edu

Ayusman Sen — Department of Chemistry, The Pennsylvania State University, University Park, Pennsylvania 16802, United States; orcid.org/0000-0002-0556-9509; Email: asen@psu.edu

Authors

Benjamin M. Tansi – Department of Chemistry, The Pennsylvania State University, University Park, Pennsylvania 16802, United States

Raj Kumar Manna — Department of Chemical Engineering, University of Pittsburgh, Pittsburgh, Pennsylvania 15213, United States; o orcid.org/0000-0003-2272-9487

Oleg E. Shklyaev – Department of Chemical Engineering, University of Pittsburgh, Pittsburgh, Pennsylvania 15213, United States

Matthew L. Peris – Department of Chemistry, The Pennsylvania State University, University Park, Pennsylvania 16802, United States

Complete contact information is available at: https://pubs.acs.org/10.1021/acsami.0c21291

Author Contributions

§B.M.T. and R.K.M. contributed equally to this study

The authors declare no competing financial interest.

ACKNOWLEDGMENTS

A.S. and A.C.B. gratefully acknowledge funding from NSF grant 1740630: CCI Phase I: Center for Chemomechanical Assembly. A.S. also acknowledges support from the Department of Energy, Office of Basic Energy Sciences (DE-SC0020964). We acknowledge the computational facilities at

the Center for Research Computing at the University of Pittsburgh.

REFERENCES

- (1) Kline, T. R.; Paxton, W. F.; Wang, Y.; Velegol, D.; Mallouk, T. E.; Sen, A. Catalytic Micropumps: Microscopic Convective Fluid Flow and Pattern Formation. *J. Am. Chem. Soc.* **2005**, *127*, 17150–17151.
- (2) Wang, W.; Zhou, C. A Journey of Nanomotors for Targeted Cancer Therapy: Principles, Challenges, and a Critical Review of the State-of-the-Art. *Adv. Healthcare Mater.* **2020**, *10*, 202001236.
- (3) Yu, T.; Athanassiadis, A. G.; Popescu, M. N.; Chikkadi, V.; Güth, A.; Singh, D. P.; Qiu, T.; Fischer, P. Microchannels with Self-Pumping Walls. ACS Nano 2020, 14, 13673.
- (4) Munteanu, R.-E.; Popescu, M. N.; Gáspár, S. The Impact of Geometrical Confinement in a Slab on the Behavior of Tracer Particles near Active Glucose Oxidase Micropump. *Colloid Polym. Sci.* **2020**, 1–10, DOI: 10.1007/s00396-020-04744-y.
- (5) Munteanu, R.-E.; Popescu, M. N.; Gáspár, S. Glucose Oxidase Micropumps: Multi-Faceted Effects of Chemical Activity on Tracer Particles Near the Solid Liquid Interface. *Condens. Matter* **2019**, *4*, 73.
- (6) Patra, D.; Sengupta, S.; Duan, W.; Zhang, H.; Pavlick, R.; Sen, A. Intelligent, Self-Powered, Drug Delivery Systems. *Nanoscale* **2013**, *5*, 1273–1283.
- (7) Zhou, C.; Zhang, H.; Li, Z.; Wang, W. Chemistry Pumps: A Review of Chemically Powered Micropumps. *Lab Chip* **2016**, *16*, 1797–1811.
- (8) Wong, F.; Dey, K. K.; Sen, A. Synthetic Micro/Nanomotors and Pumps: Fabrication and Applications. *Annu. Rev. Mater. Res.* **2016**, *46*, 407.
- (9) Alistar, M. Mobile Microfluidics. Bioengineering 2019, 6, 5.
- (10) Yadav, V.; Zhang, H.; Pavlick, R.; Sen, A. Triggered "On/Off" Micropumps and Colloidal Photodiode. J. Am. Chem. Soc. 2012, 134, 15688.
- (11) Donner, J. S.; Baffou, G.; McCloskey, D.; Quidant, R. Plasmon-Assisted Optofluidics. ACS Nano 2011, 5, 5457–5462.
- (12) Li, M.; Su, Y.; Zhang, H.; Dong, B. Light-Powered Direction-Controlled Micropump. *Nano Res.* **2018**, *11*, 1810.
- (13) Tansi, B. M.; Peris, M. L.; Shklyaev, O. E.; Balazs, A. C.; Sen, A. Organization of Particle Islands through Light-Powered Fluid Pumping. *Angew. Chem., Int. Ed.* **2019**, *58*, 2295–2299.
- (14) Manna, R. K.; Shklyaev, O. E.; Kauffman, J.; Tansi, B.; Sen, A.; Balazs, A. C. Light-Induced Convective Segregation of Different Sized Microparticles. *ACS Appl. Mater. Interfaces* **2019**, *11*, 18004–18012.
- (15) Sengupta, S.; Patra, D.; Ortiz-Rivera, I.; Agrawal, A.; Shklyaev, S.; Dey, K. K.; Córdova-Figueroa, U.; Mallouk, T. E.; Sen, A. Self-Powered Enzyme Micropumps. *Nat. Chem.* **2014**, *6*, 415–422.
- (16) Derjaguin, B. V.; Sidorenkov, G. P.; Zubashchenkov, E. A.; Kiseleva, E. V. Kinetic Phenomena in Boundary Films of Liquids. *Kolloidn. Zh.* **1947**, *9*, 335.
- (17) Anderson, J. L. Colloid Transport By Interfacial Forces. *Annu. Rev. Fluid. Mech.* **1989**, 21, 61–99.
- (18) Bhagat, A. A. S.; Bow, H.; Hou, H. W.; Tan, S. J.; Han, J.; Lim, C. T. Microfluidics for Cell Separation. *Med. Biol. Eng. Comput.* **2010**, 48, 999–1014.
- (19) Maiti, S.; Shklyaev, O. E.; Balazs, A. C.; Sen, A. Self-Organization of Fluids in a Multi-Enzymatic Pump System. *Langmuir* **2019**, 35, 3724–3732.
- (20) Ortiz-Rivera, I.; Shum, H.; Agrawal, A.; Sen, A.; Balazs, A. C. Convective Flow Reversal in Self-Powered Enzyme Micropumps. *Proc. Natl. Acad. Sci. U.S.A.* **2016**, *113*, 2585–2590.
- (21) Bothe, E.; Schuchmann, M. N.; Schulte-Frohlinde, D.; Sonntag, C. v. Hydroxyl Radical-Induced Oxidation of Ethanol in Oxygenated Aqueous Solutions. A Pulse Radiolysis and Product Study. Z. Naturforsch., B: Chem. Sci. 1983, 38, 212–219.
- (22) Cataldo, F. Hydrogen Peroxide Photolysis with Different UV Light Sources Including a New UV-LED Light Source. *New Front. Chem.* **2014**, 23, 99.

- (23) Chandrasekhar, S. Hydrodynamic and Hydromagnetic Stability; Courier Corporation, 2013.
- (24) Keh, H. J.; Ma, H. C. Diffusioosmosis of Electrolyte Solutions along a Charged Plane Wall. *Langmuir* **2005**, *21*, 5461–5467.
- (25) Shum, H.; Balazs, A. C. Flow-Driven Assembly of Microcapsules into Three-Dimensional Towers. *Langmuir* **2018**, *34*, 2890–2899.
- (26) Oron, A.; Davis, S. H.; Bankoff, S. G. Long-Scale Evolution of Thin Liquid Films. *Rev. Mod. Phys.* **1997**, *69*, 931–980.
- (27) Tavakol, B.; Froehlicher, G.; Holmes, D. P.; Stone, H. A. Extended Lubrication Theory: Improved Estimates of Flow in Channels with Variable Geometry. *Proc. R. Soc. A* **2017**, 473, 20170234.
- (28) Leal, L. G. Laminar Flow and Convective Transport Processes; Elsevier, 1992; Vol. 251.
- (29) Prieve, D. C.; Roman, R. Diffusiophoresis of a Rigid Sphere through a Viscous Electrolyte Solution. *J. Chem. Soc., Faraday Trans.* 2 1987, 83, 1287–1306.
- (30) Prieve, D. C.; Anderson, J. L.; Ebel, J. P.; Lowell, M. E. Motion of a Particle Generated by Chemical Gradients Part 2 Eelectrolytes. *J. Fluid Mech.* **1984**, *148*, 247–269.
- (31) Shin, S.; Um, E.; Sabass, B.; Ault, J. T.; Rahimi, M.; Warren, P. B.; Stone, H. A. Size-Dependent Control of Colloid Transport via Solute Gradients in Dead-End Channels. *Proc. Natl. Acad. Sci. U.S.A.* **2016**, *113*, 257–261.